Journal Pre-proof

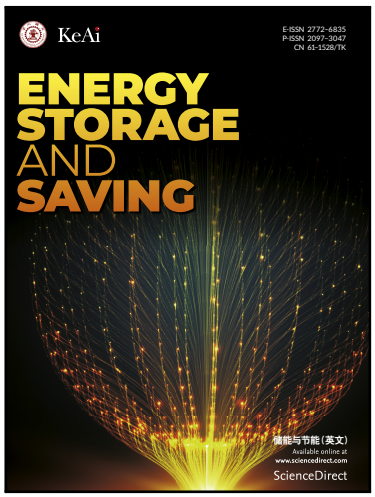

Simulation Design and Optimization of Reactors for Carbon Dioxide Mineralization

Duoyong Zhang , Chen Zhang , Tao Xuan , Xinqi Zhang , Liwei Wang , Yongqiang Tian , Jinqing Zhu

PII: S2772-6835(24)00016-5
DOI: https://doi.org/10.1016/j.enss.2024.04.002
Reference: ENSS 72

To appear in: *Energy Storage and Saving*

Received date: 15 January 2024
Revised date: 25 April 2024
Accepted date: 28 April 2024

Please cite this article as: Duoyong Zhang , Chen Zhang , Tao Xuan , Xinqi Zhang , Liwei Wang , Yongqiang Tian , Jinqing Zhu , Simulation Design and Optimization of Reactors for Carbon Dioxide Mineralization, *Energy Storage and Saving* (2024), doi: https://doi.org/10.1016/j.enss.2024.04.002

Simulation Design and Optimization of Reactors for Carbon Dioxide Mineralization

Duoyong Zhang[1,2], Chen Zhang[1,2], Tao Xuan[1,2], Xinqi Zhang[2,3], Liwei Wang[1,2,*]

Yongqiang Tian[4,5], Jinqing Zhu[4,5]

1.Institute of Refrigeration and Cryogenics, Key Laboratory of Power Machinery and Engineering of MOE, Shanghai Jiao Tong University, Shanghai, 200240, China

2. Shanghai Non-carbon energy conversion and utilization institute, Shanghai 200240, China

3.China-UK Low Carbon College, Shanghai Jiao Tong University, Shanghai, 201306, China

4 SPIC Xinjiang Energy Chemical CO., LTD., Urumqi, Xinjiang 830000, China

5 SPIC Xinjiang Wucaiwan Power Generation Co., LTD., Changji, Xinjiang 831100, China

*Liwei Wang: lwwang@sjtu.edu.cn

Abstract

To achieve a synergistic solution for both sustainable waste management and permanent CO_2 sequestration, CO_2 mineralization via fly ash particles is an option. Based on computational fluid dynamics, two specialized reactors for fly ash mineralization were designed. The reactor designs were strategically tailored to optimize the interactions between fly ash particles and flue gas within the reactor chamber while concurrently facilitating efficient post-reaction-phase separation. The impinging-type inlet configuration dramatically enhanced the interfacial interaction

between the fly ash particles and the gaseous mixture, predominantly composed of CO_2 and steam. This design modality lengthens the particle residency and reaction times, substantially augmenting the mineralization efficiency. A rigorous investigation of three operational parameters, that is, flue gas velocity, carrier gas velocity, and particle velocity, revealed their influential roles in gas-particle contact kinetics. Through a computational investigation, it can be ascertained that the optimal velocity regime for the flue gas was between 20 and 25 $m \cdot s^{-1}$. Concurrently, the carrier gas velocity should be confined to the range of 9–15 $m \cdot s^{-1}$. Operating within these finely tuned parameters engenders a marked enhancement in reactor performance, thereby providing a robust theoretical basis for operational efficacy. Overall, a judicious reactor design was integrated with data-driven parameter optimization.

Keywords: CO_2 mineralization; Mass transfer; Flow field; Particle trajectory

Graphical abstract

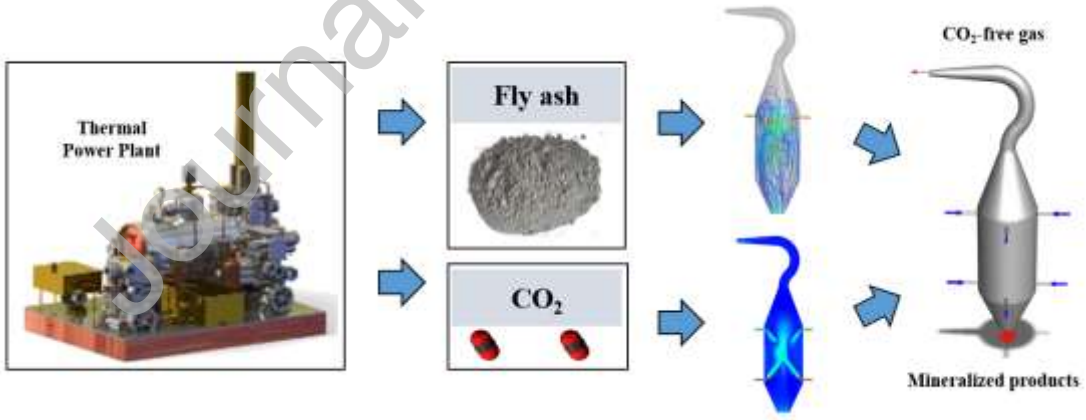

1 Introduction

As industrialization advances, the exploitation and consumption of fossil fuels have escalated carbon dioxide emissions. These emissions are the primary drivers of

the greenhouse effect, contributing to global warming and rising sea levels, and thereby imperiling vital environmental conditions for human existence. The emissions, predominantly stemming from industrial fossil fuel combustion, necessitate urgent measures for carbon capture, utilization, and storage (CCUS) [1].

CCUS currently comprises CO_2 capture, transportation, utilization, and storage. Carbon dioxide capture methods are divided into pre- and post-combustion techniques, and further categorized into liquid absorption [2−4] and solid adsorption [5,6]. CO_2 utilization and storage aim to repurpose captured CO_2 for chemical, geological, and biological applications [7].

Carbon dioxide mineralization technology integrates CO_2 capture and utilization, addressing the low utilization rates and resource waste of fly ash in coal-based heat engine plant solid wastes. By facilitating chemical reactions between fly ash rich in CaO and MgO and carbon dioxide, this process transforms CaO into $CaCO_3$, finding applications in construction and contributing to on-site industrial CO_2 stabilization for emission reduction [8−11]. This not only accomplishes the reuse of fly ash waste but also stabilizes on-site industrial CO_2, thereby achieving the objective of reducing carbon emissions [12−14]. Pioneering techniques, such as the CO_2 adsorption mineralization method by Ji et al. [15], exhibit energy and cost efficiencies, but require further refinement, especially in product detoxification and industrial-scale deployment.

Within the contemporary technological framework of CO_2 mineralization, methodologies are predominantly divided into dry and wet mineralization strategies, with the moisture content during the reaction serving as a pivotal discriminator [16]. Typically, flue gases from thermal power plants exhibit substantial moisture profiles, although predominantly in the form of steam. Zevenhoven et al. [17] investigated CO_2 mineralization using Mg-based materials. Although they identified the optimal temperature and pressure conditions, the nuances of reactor design in practical settings

require further exploration. Ukwattage et al. [18] examined the CO_2 mineralization potential of fly ash. Their focus was on key parameters such as the effect of CO_2 pressure on adsorption and the influence of water-to-solid ratios on post-carbonization weight gain. However, the study lacked a detailed applicative groundwork. To date, the design architecture of reactors for CO_2 mineralization has evolved to encompass a myriad of structures, including bubble column reactors [19−22], rotating disk reactors [23,24], fixed-bed reactors [25,26], and fluidized-bed reactors [27−31]. The latter has attracted particular attention owing to its efficient heat and mass transfer capabilities, continuous processing of materials on a substantial scale, stellar dynamic adjustment capabilities, and the ability to mitigate particle aggregation. These attributes unfurl significant potential and prospects for application and development in the field [32]. By leveraging the Euler–Lagrangian one-way coupling approach, Legendre et al. [33] proficiently simulated the gas-liquid biphasic coupling dynamics within bubble columns. Their contributions enrich the numerical modeling landscape of the mineralization process. However, a comprehensive examination of the reactor parameters and their optimization remained conspicuously absent from their investigations. Guo [34] used potassium-based solid adsorbents in fixed-bed reactors to probe the CO_2 adsorption dynamics, mechanisms, rejuvenation potential, and multi-cycle traits. However, the capability of these reactors to persistently manage large fluxes of gases and waste requires heightened optimization and fortification.

The use of fly ash, an industrial waste material, for CO_2 mineralization within fluidized beds presents a kinetic challenge. Specifically, the intricate activation of CO_2 with calcium- and magnesium-based solid wastes poses significant hurdles for its effective utilization, forming a substantial barrier to the realization of this process.

This study aims to address the existing limitations of gas-particle interactions within modern fluidized-bed reactors. Through numerical simulations, a multiphase fluidized bed specifically tailored for the mineralization process was devised,

enabling a thorough analysis of the optimal reactive mixtures and material separation flow fields to enhance the reactor efficiency. The goal was to optimize the synergistic interplay between fly ash particles and flue gas constituents, facilitating effective CO_2 mineralization while ensuring post-reaction phase separation. Additionally, this research meticulously evaluated the impact of optimal parameters, including a multistream CO_2 inlet and fly ash feeding, on the gas-particle interaction process, paving the way for efficient waste reuse and carbon reduction.

2. Reactor design and simulation computational methods

To address the conundrum of fly ash and carbon dioxide emissions in thermal power plants, the reactor architectural process strategically considers the incorporation of fly ash and flue gas ingress points, culminating in a meticulously engineered reactor model tailored for CO_2 mineralization, the conceptual framework of which is depicted in the graphical abstract. Within this schema, we conducted a numerical analysis of both gaseous (flue gas) and solid (fly ash) phases, thereby offering a holistic understanding of their synergistic interactions within the reactor environment.

2.1 Reactor design

Two unique reactor designs are presented, each featuring eight strategically positioned inlets in the mid-section of the reactor. The upper quadrant had four inlets for the introduction of fly ash particles, whereas the lower quadrant contained four inlets designed for the intake of the gaseous phase enriched with carbon dioxide and steam. An outlet at the top of the reactor allowed the release of the post-reaction gaseous phase. The conduit of this outlet was intentionally curved to increase path resistance and minimize the potential release of fly ash particles. An exit at the base of the reactor facilitated the discharge of post-reaction fly ash particles.

To optimize performance, two reactor designs were explored, differing mainly in

the angle and method of reactant introduction. The first approach employs an impinging-style inlet configuration; upon entry, the reactor nozzles are angled at 30°. The upper four nozzles bent downwards, whereas their lower counterparts flexed upward, ensuring that the projected paths of all eight nozzles converged at the core of the reactor. This arrangement guarantees thorough mixing and contact between the gaseous and solid phases, although with a more intricate flow pattern. Conversely, the second design used a quadrilateral rotary-style inlet, with the eight tubes entering the reactor at a 45° angle, diverging from a direct vertical alignment. Similarly, upon entry, both the upper and lower nozzles were angled at 30°. This setup facilitated the mixing and reaction of the gas and solid phases around the reactor perimeter, resulting in comparatively streamlined flow dynamics.

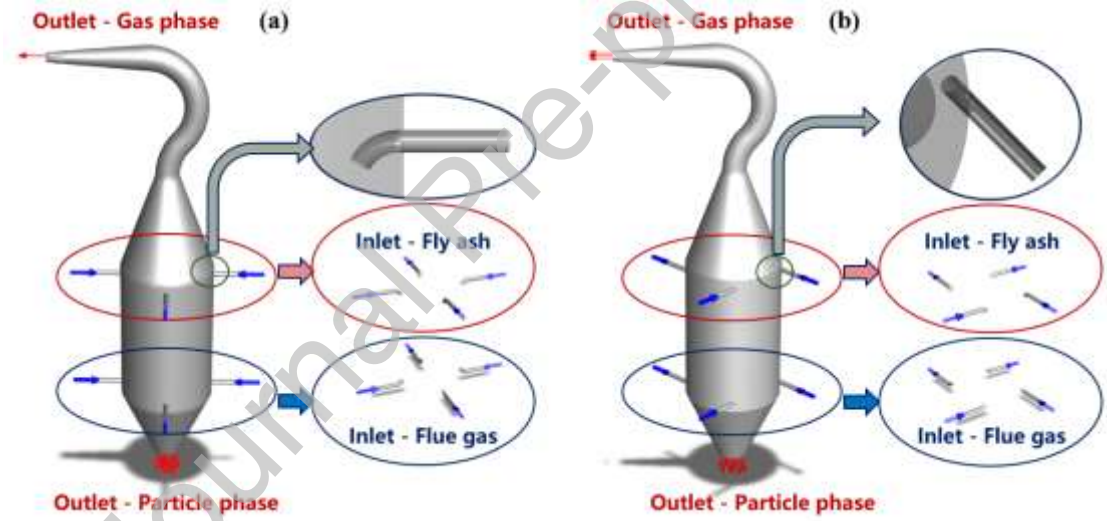

Fig. 1. Comparative schematics of two distinct reactor design strategies. (a) Impinging-style inlet design; (b) quadrilateral rotary-style inlet design.

In both reactors, fly ash, a by-product of power plants, and carbon dioxide from the emitted flue gas undergo mixing and reactions. Disparities in the configuration of flow channels lead to substantial variations in the regions and patterns of the internal gas-particle two-phase flow. This divergence ultimately gives rise to distinct contact

effects between the gas and particles, thereby influencing the outcome of mineralization. Consequently, in this study, computations tailored to the flow processes in two distinct reactors were performed.

2.2 Simulation methods

2.2.1 Discrete phase model (DPM)

The fly ash particles were sprayed into the reactor through the inlets and reacted with the CO_2. The DPM was used to describe the fly ash particle motion process; specifically, the trajectory of the fly ash particles was tracked using the Lagrangian method [35–37].

Newton's second law of motion:

$$m_p \frac{\mathrm{d}\boldsymbol{u_p}}{\mathrm{d}t} = m_p F_D\left(\boldsymbol{u}-\boldsymbol{u_P}\right) + m_p \frac{\boldsymbol{g}\left(\rho_p-\rho\right)}{\rho_p} \tag{1}$$

where $F_D\left(\boldsymbol{u}-\boldsymbol{u_P}\right)$ is the traction force per unit mass of the particle, where the expression F_D is expressed as

$$F_D = \frac{18\mu}{\rho_p d_p^2}\frac{C_D Re}{24} \tag{2}$$

where m_p is the mass of the particle; $\boldsymbol{u}$ is the gas-phase velocity; $\boldsymbol{u_P}$ is the particle velocity; μ is the molecular dynamic viscosity of the gas phase; ρ is the gas-phase density; ρ_p is the particle density; $\boldsymbol{d}_p$ is the particle diameter; and Re is the Reynolds number of the particle.

2.2.2 Gas-phase transport model

CO_2, steam, and the carrier gases were injected into the reactor. The gas-phase transfer process is described by the following control equation:

Continuity equation:

$$\frac{\partial \rho}{\partial t} + \nabla \cdot (\rho \boldsymbol{u}) = S_m \tag{3}$$

where ρ is the gas density and S_m represents the gas-phase mass source term, which in this context is determined to be 0.

Momentum equation:

$$\frac{\partial (\rho \boldsymbol{u})}{\partial t} + \nabla \cdot (\rho \boldsymbol{u}\boldsymbol{u}) = -\nabla p + \nabla \cdot \left[(\mu + \mu_t) \cdot \left(\nabla \boldsymbol{u} + (\nabla \boldsymbol{u})^T \right) \right] + \boldsymbol{f} \tag{4}$$

where g is the acceleration due to gravity, f_i represents the force between the fly ash and gas phases.

Owing to the high velocity of the gas phase in the reactor, which is a turbulent flow, the flow of the gas phase was numerically simulated using the standard turbulent k-ε model:

k -equation：

$$\frac{\partial}{\partial t}(\rho k) + \frac{\partial}{\partial x_i}(\rho k u_i) = \frac{\partial}{\partial x_j}\left[\left(\mu + \frac{\mu_t}{\sigma_k} \right) \frac{\partial k}{\partial x_j} \right] + G_k + G_b - \rho \varepsilon - Y_M + S_k \tag{5}$$

ε -equation：

$$\frac{\partial}{\partial t}(\rho \varepsilon) + \frac{\partial}{\partial x_i}(\rho \varepsilon u_i) = \frac{\partial}{\partial x_j}\left[\left(\mu + \frac{\mu_t}{\sigma_\varepsilon} \right) \frac{\partial \varepsilon}{\partial x_j} \right] + C_{1\varepsilon} \frac{\varepsilon}{k} (G_k + C_{3\varepsilon} G_b) - C_{2\varepsilon} \rho \frac{\varepsilon^2}{k} + S_\varepsilon \tag{6}$$

where k is the turbulent kinetic energy, ε is the turbulent energy dissipation rate, and μ_t is the turbulent viscosity.

To strike a balance between computational efficiency and numerical accuracy, first-order upwind was strategically employed for the quantification of turbulent kinetic energy and turbulent dissipation rate in the simulations. Furthermore, the simulations

used second-order upwind for momentum equations and the Green-Gauss method for gradient calculations.

To ensure that the computational process aligns with industrial field conditions, the setup of the relevant initial conditions is shown in Table 1.

Table 1 Simulation parameters

Variable	Value
Density of fly ash particles	2.1 g·cm^{-3}
Density of flue gas	1.296 kg·m^{-3}
Velocity of carrier gas	12 m·s^{-1}
Velocity of flue gas	20 m·s^{-1}
Components of flue gas	14% CO_2, 10% H_2O, 76% N_2
Temperature of flue gas	308 K
Pressure of inlets	−464 Pa

Temperature variations are disregarded in the calculations, along with the influence of chemical reactions on the two-phase flow process. The outlet boundary conditions are set as outflow. The particle size distribution of fly ash particles ranges from 80 μm to 150 μm, with mass distributions of 80 μm (20%), 100 μm (50%), 120 μm (20%), and 150 μm (10%).

In an endeavor to rigorously assess the models, we scrutinized a range of grid densities with respective mesh counts of 0.8, 1.8, 2.4, 3.4, and 4.2 million. Taking the velocity along the central axis of the reactor as a reference metric, the relative errors for the initial four meshes were calculated to be 9.7%, 3.2%, 1.6%, and 0.5%. To balance

computational precision and efficiency judiciously, simulations were carried out employing a mesh count of 2.4 million for all subsequent analyses. In all calculations of the models and operating conditions in this study, the residual settings were set to 10^{-6} to ensure computational precision.

3 Results and discussion

3.1 Influence on two types of reactors

Key data encompassing the particle trajectory and gas-phase velocity were acquired, enabling a comprehensive comparative analysis of the two reactors featuring distinct inlet configurations. The concept of particle residence time was introduced to portray the mineralization effect more accurately. This refers to the duration that the particles spend within the reactor, from their entry at the inlet to their exit at the outlet, and encompasses the intermediate residence time within the reactor. In the impinging-style inlet design, the particles exhibited an oscillatory motion pattern under the influence of airflow dynamics. In Fig. 2(a), the uppermost pair of diagrams offers a front perspective of the particle trajectories, whereas the lower pair provides an overhead vantage point. Upon their introduction into the reactor, the particles initially ascended owing to the propulsive force of the high-velocity upward airstream, thereby facilitating the initial phase of extensive mixing and contact. Subsequently, under the influence of positive pressure, frictional forces, and gravitational effects, these particles traverse downward along the inner reactor wall. Upon reaching the lower gas-phase inlet position, they underwent a renewed ascent, propelled by airflow pressure, and subsequently returned to the mid-section of the reactor. Thereafter, they continued to descend along the inner reactor wall, achieving a secondary phase of thorough mixing and contact. The two rightmost diagrams in Fig. 2(a) show the trajectories of particles ejected from a single outlet, underscoring the efficacy of the impaction-type reactor and its nozzle design in ameliorating issues related to inadequate and non-uniform

gas-particle contact during particle movement. This effectively prolonged the particle residence time within the reactor, thereby significantly enhancing the mineralization process. Fig. 2(c) shows the gas-phase velocity distributions in the two reactors. In the impinging-type reactor on the left, notably along the nozzle axis and at the central position of the reactor, higher velocities were observed, whereas the velocities in other regions were diminished.

Fig. 2(b) illustrates the motion of particles along their trajectories in a reactor equipped with a quadrilateral rotary-style inlet. Influenced by their initial velocities and the flow of the flue gas, the particles exhibited a relatively organized motion pattern as they circulated within the reactor. Over time, following their introduction into the reactor, the particle velocities gradually increased, accelerating their exit from the base of the reactor. As depicted in the rightmost diagram of Fig. 2c, the quadrilateral rotary-style reactor design predominantly concentrates on high-velocity regions along the peripheral wall, whereas the central region at the vortex core displays comparatively lower velocities. Nevertheless, the flow field within a quadrilateral rotary-style reactor raises concerns regarding heightened fluid shear stresses at the wall locations, resulting in increased friction that could potentially impact the operational lifespan of the reactor.

As shown in Fig. 2, the first nozzle design configuration engendered a markedly elevated relative velocity between the gas and the particles when juxtaposed with the second design schema. To quantify this impact, we rigorously assessed the effective contact duration between the particulates and flue gas within the reactor milieu. Our findings show that the effective contact time under the first nozzle configuration is an astounding 7.9 times greater than that of its counterpart, thereby emphatically corroborating the preeminence of the first design in facilitating enhanced mineralization efficacy.

To enhance the mineralization efficiency and ensure adequate contact time

between the fly ash particles and flue gas flow, enhancing turbulence and reinforcing the contact process have emerged as critical objectives. The design of the impinging-type reactor inlet represents a strategy specifically aimed at streamlining the mineralization process. Simultaneously, the impinging-type reactor holds promise for extending the operational lifespan. Consequently, this study is dedicated to utilizing this reactor design, with forthcoming research endeavors dedicated to optimization.

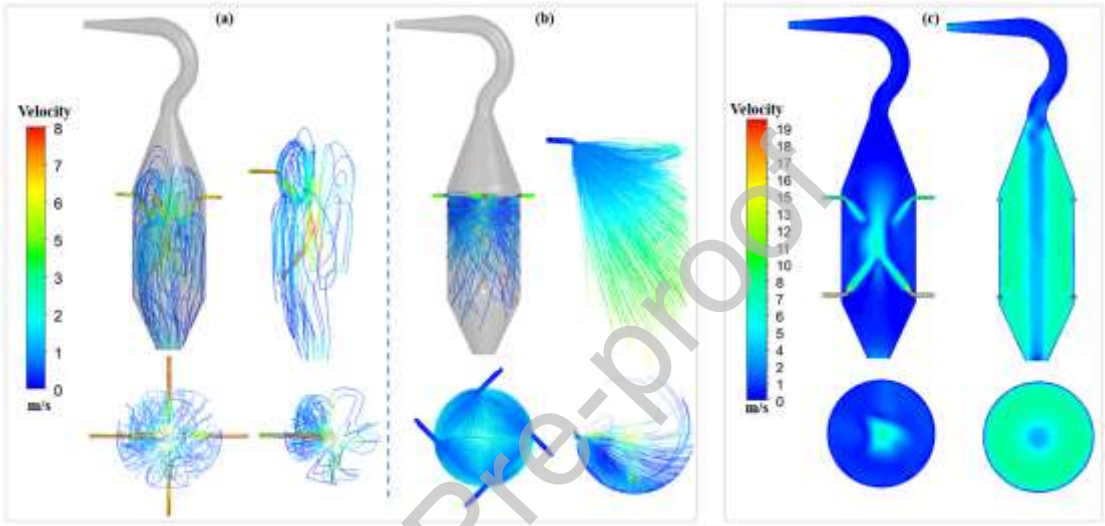

Fig. 2. (a) Particle movement trajectories within the impinging-type reactor; (b) particle trajectories within the quadrilateral rotary-style circular-type reactor; (c) flow field distributions within both reactor configurations.

Given the challenges associated with adjusting parameters such as pressure in industrial production settings, the optimization process in this study does not involve pressure-related variables. Instead, the primary focus was on investigating the impact of flue gas, fly ash particles, and carrier gas on the internal gas-particle two-phase flow and contact processes within the reactor.

3.2 Optimization of gas-phase velocity

The gases entering the gas-phase inlet primarily consist of flue gas from the power

plant after desulfurization and denitrification, comprising predominantly nitrogen, carbon dioxide, water vapor, and other constituents. As the main medium driving the reactions, optimization of the reactor critically relies on the characteristics of the flue gas.

In this section, we delve into the profound impact of the flue gas inlet velocity on the critical factors influencing the mineralization process, including the level of gas-particle mixing, contact conditions, and particle residence time. To maintain consistency, the particle and carrier gas feed rates were kept constant, while the flue gas velocity was systematically adjusted from 10 to 30 $m \cdot s^{-1}$. Simulations were conducted at intervals of 5 $m \cdot s^{-1}$.

Figs. 3(a) and 3(b) show front- and top-down perspectives of the distribution of the gas-phase velocity within the reactor. Fig. 3(c) shows the level of fluid–particle mixing through the turbulence eddy dissipation rate, while Fig. 3d shows the particle trajectories subsequent to their ingress into the reactor. Significantly, an increase in the velocity of the flue gas correlated with a pronounced surge in velocity at the center of the reactor, thereby augmenting the vertical momentum. Simultaneously, the turbulence eddy dissipation rate in the vicinity of the flue gas nozzle and reactor core increased, which can be attributed to elevated gas-phase scouring dynamics.

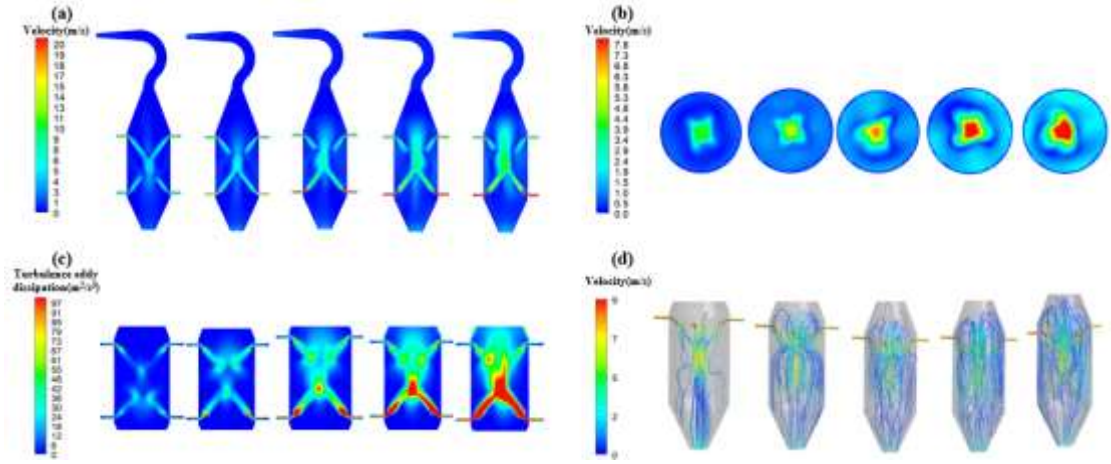

Fig. 3. Calculation results at different gas-phase velocities. (a) Front perspective of the velocity distribution; (b) top-down perspective of the velocity distribution; (c) turbulence eddy dissipation rate in the mid-section of the reactor; (d) trajectories of fly ash particles.

In the fly ash particle trajectory analysis presented in Fig. 3, the influence of disparate flue gas velocities on particle behavior is elucidated. At a suboptimal velocity of 10 $m \cdot s^{-1}$, the particles engaged in a paucity of effective collisions with the flue gas in the center of the reactor, largely bypassing it to egress unimpeded. The minuscule fraction of particles was influenced by the fluid dynamics that meander toward the reactor walls, descending along them under the influence of gravity. Consequently, these suboptimal velocities are associated with attenuated gas-particle interactions and compromised mineralization efficacy.

As the flue gas velocity increased to 15 $m \cdot s^{-1}$, a subset of the particles underwent an inaugural upward gyration within the center of the reactor. However, residual particles continued to exit directly, indicating further avenues for the optimization of biphasic flow and interaction. An incremental elevation of the gas velocity to 20 $m \cdot s^{-1}$ resulted in more comprehensive bidirectional mixing and particle-gas contact, and the effective residence time of the particles experienced a 4.2-fold increase compared to the conditions at a flow rate of 10 $m \cdot s^{-1}$, thereby amplifying mineralization proficiency.

However, it is important to emphasize the detrimental repercussions of excessively high flue gas velocities. Elevated rates carry the latent risk of particle egress from the apex vent, thus deleteriously impacting gas-particle-phase separation and concomitantly truncating the longevity of the reactor. Consequently, rigorous calibration of the flue gas velocity is indispensable to forestall excessive or inordinate flow rates.

To enable sophisticated analysis and empirical scrutiny, four axial monitoring characteristic lines at discrete radial distances were carefully placed within the geometrical framework of the reactor. These characteristic lines were positioned along the axial centerline as well as at one-quarter, one-half, and three-quarters of the reactor core radius, as shown in Fig. 4a. Subsequently, gas-phase velocity metrics were harvested from each axial transect, yielding correlative graphical representations, as shown in Figs. 4(b)–4(e).

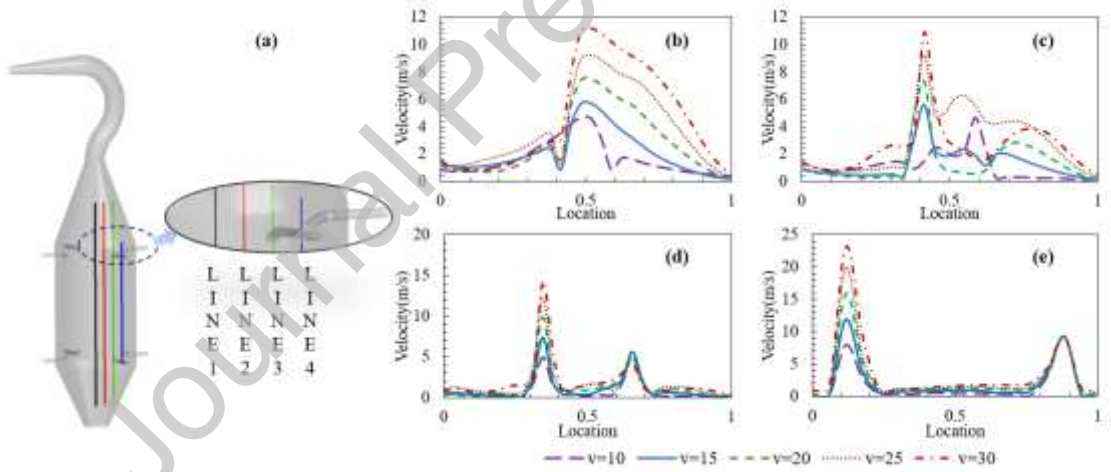

Fig. 4. Velocity distribution on characteristic lines at different gas-phase velocities. (a) Line position; (b) line 1; (c) line 2; (d) line 3; (e) line 4.

An exhaustive analysis of the velocity profiles along the axial centerline of the reactor revealed distinct flow patterns. At the base of the reactor, markedly reduced flow velocities were observed, with the vertical components measuring only 0.067

$m \cdot s^{-1}$, which is particularly conducive for the effective separation of flue gases and fly ash particles. In contrast, the central and upper sections of the reactor experienced an initial surge in gas-phase velocity that was eventually moderated, a trend that significantly advanced the mineralization process.

Focusing on the radial velocity profiles, which extend from one-quarter to three-quarters of the reactor core radius, it can be observed that the zones of elevated velocity are predominantly aligned with the gas-particle nozzle trajectories. This characteristic intensifies near the wall boundaries, creating a flow field that is uniquely optimized to facilitate superior gas-particle interactions and prolong the particle residence time within the reactor.

3.3 Optimization of particle velocity

Fly ash particles, which serve as the primary matter in the mineralization reactions, were injected into the reactor via the four upper inlets. Consequently, the injection speed at the particle entrance, as a pivotal boundary condition, is a key parameter that influences the particle motion within the reactor and the subsequent mineralization efficiency. This study probes the intrinsic linkage between particle injection velocity and internal reactor flow dynamics. Outcomes were computationally elucidated under distinct operational scenarios with particle injection speeds of 2, 4, 6, 8, and 10 $m \cdot s^{-1}$, keeping all other conditions constant. Visualized results are delineated in Fig. 5.

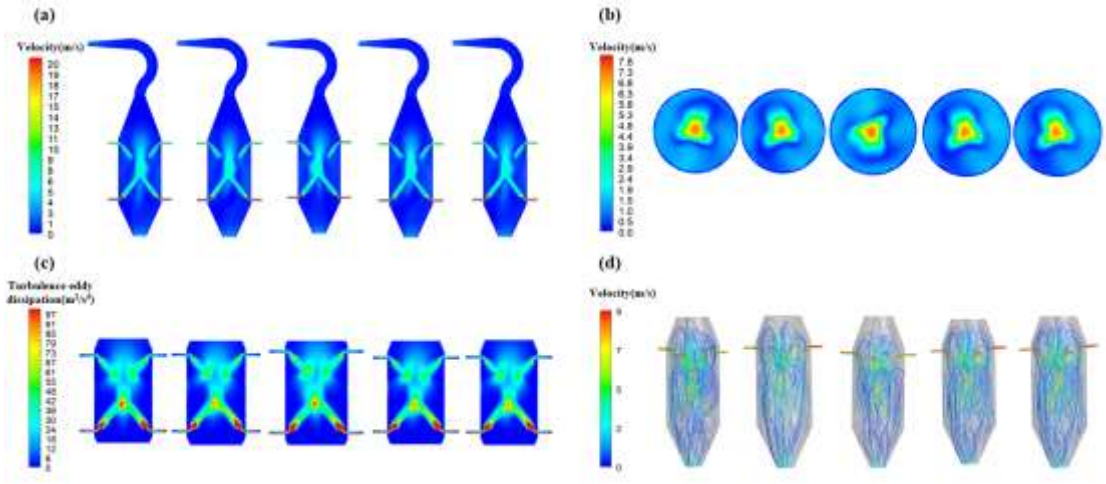

Fig. 5. Calculation results at different particle velocities. (a) Front perspective of the velocity distribution; (b) top-down perspective of the velocity distribution; (c) turbulence eddy dissipation rate in the mid-section of the reactor; (d) trajectories of fly ash particles.

Analytical insights reveal that the initial velocity of the particles has a discernible effect on turbulent eddy dissipation within the reactor flow domain, a phenomenon most prominent near the particle injection zone. Further analysis revealed that a decreased particle velocity engendered enhanced upward turbulence in the upper stratum of the reactor, largely owing to the reduced downward momentum of the particles, thereby making them more amenable to the dynamic influences of the rising flue gas currents. However, from a macroscopic perspective, the particle velocity manifests as a relatively inert parameter, imparting only marginal effects on the internal flow dynamics of the reactor.

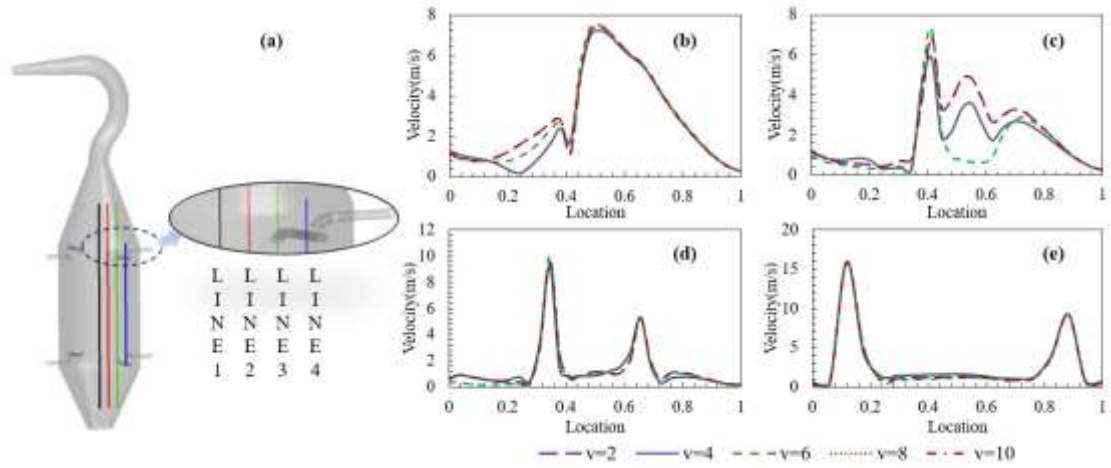

Fig. 6. Velocity distribution on characteristic lines at different particle velocities. (a) Line position; (b) line 1; (c) line 2; (d) line 3; (e) line 4.

Fig. 6 shows that the particulate velocity had minimal impact on the velocity contours mapped along the intrinsic pathways within the reactor architecture. Notably, along the axial centerline of the reactor, zones of augmented flow velocity were conspicuously confined to the mid-upper echelons, whereas the remainder of the spatial extent exhibited relatively attenuated flow dynamics.

During the practical course of production, it is imperative to consider the gas-phase velocity to calculate and subsequently extrapolate the quantity of fly ash necessary for a complete reaction. This process helps to precisely determine the inlet velocity of the fly ash, thereby fostering conducive conditions for the thorough completion of the reaction.

3.4 Optimization of carrier gas velocity

In this study, the carrier gas served as a critical conduit for the transfer of fly ash particles to the reactor, originating primarily from the fraction of gases generated post-mineralization. Utilizing a recursive transport scheme enabled by the carrier gas, these particles were effectively pushed into the operational sphere of the reactor. This

cyclic reuse strategy confers multiple benefits, most notably, enabling the secondary mineralization of residual unreacted CO_2 in exhaust flue gases, thus making a tangible contribution to CO_2 emission reduction. Furthermore, the carrier gas facilitates a preparatory mixing phase with the particulates before their entry into the reactor, thereby optimizing particle dispersion and amplifying gas-particle interfacial contacts, which is highly conducive to the acceleration of mineralization processes.

In recognition of its pivotal role as a vector for transporting fly ash particles, the carrier gas velocity exerts a significant influence on the internal mixing dynamics and fluid velocity profiles of the reactor. To elucidate these critical dependencies, the present analysis focused on the impact of variable carrier gas velocities on fluid dynamics. Computational and analytical assessments were rigorously conducted across a range of carrier gas velocities, specifically 6, 9, 12, 15, and 18 $m \cdot s^{-1}$, with the flue gas velocity held constant. The comprehensive results of these evaluations are delineated in Fig. 7.

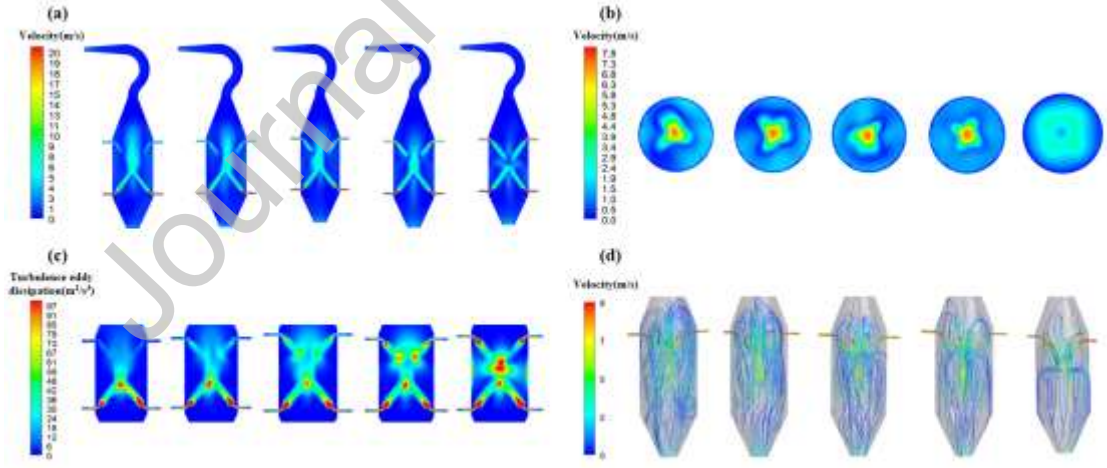

Fig. 7. Calculation results at different carrier gas velocities. (a) Front perspective of the velocity distribution; (b) top-down perspective of the velocity distribution; (c) turbulence eddy dissipation rate in the mid-section of the reactor; (d) trajectories of fly ash particles.

Fig. 7 shows the consequential interplay between the enhanced carrier gas velocity and augmentation of the flow speed proximal to the particle-phase nozzle alignment, amplifying the turbulent energy dissipation at the central locus of the reactor. A notable manifestation occurs as the carrier gas velocity ascends to 18 $m \cdot s^{-1}$, where a perceptible "stagnation zone" materializes within the mid-sector of the reactor. Within this domain, the collective force derived from the aerodynamic output of the eight nozzles converges towards nullity, thereby culminating in a relatively stable kinematic state for the biphasic gas-particle system at this juncture. Before approaching this “stagnation zone”, fly ash particles, propelled by the prevailing gas currents, diffuse radially, subsequently descending along the reactor wall upon intersection and ultimately vacating the reactor. This dynamic leads to a brief reaction duration and insufficient mixing, resulting in suboptimal mineralization outcomes. Further scrutiny asserts that the carrier gas velocity should not exceed 18 $m \cdot s^{-1}$, as breaching this velocity parameter induces a downward trajectory of the integral momentum of the entrant gas-particle system within the reactor, precipitating a profuse egress of particles from the lower particle outlet, thwarting not only product separation but also severely compromising reactor operability.

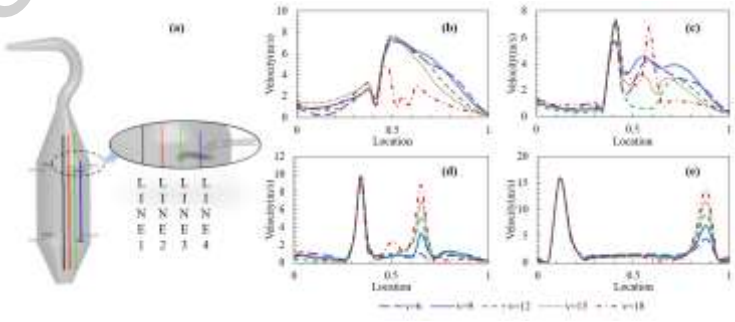

Fig. 8. Velocity distribution on characteristic lines at different carrier gas velocities. (a) Line position; (b) line 1; (c) line 2; (d) line 3; (e) line 4.

In scenarios where the carrier gas velocity was fixed at 6 $m \cdot s^{-1}$ and the smoke gas flow speed markedly superseded that of the carrier gas, coal ash particles in the upper echelon of the reactor were facilitated to achieve thorough mixing and protracted dwell and interaction times. However, the monitoring outcomes from the gas phase exit indicate the subtle escape of a minor fraction of coal ash particles from the system, a phenomenon detracting from the efficacy of the subsequent gas-particle separation process.

When the carrier gas velocity resides within the 9-15 $m \cdot s^{-1}$ interval, the motion trajectory of the biphasic gas-particle system exhibits notable stability. Within this ambit, an escalation in the carrier gas velocity concurrently intensified the impinging action of the flue gas on the surface of the coal ash particles.

Fig. 8, illustrated by the velocity distribution along four characteristic lines, provides insight into this phenomenon. While the increased carrier gas velocity has a minimal impact on the gas-phase velocity distribution in the initial segment, it significantly influences the velocity distribution in the lower portion.

Considering the aforementioned insights, to safeguard the operation of the reactor within a normative and efficacious operational envelope, it is prudent to confine the carrier gas inlet velocity within a 9–15 $m \cdot s^{-1}$ spectrum, while judiciously averting overly intensified or attenuated velocities.

4 Conclusions

In conclusion, our study has introduced a novel fluidized-bed reactor designed to capture carbon dioxide from flue gas during the mineralization process of coal fly ash. In this study, the meticulously calculated injector design significantly enhanced gas-solid contact processes. Compared with conventional inlet designs, the impinging-style inlet reactor prolongs the particle residence time by up to 7.9 times, thereby facilitating the mineralization process of coal fly ash. Additionally, we

conducted optimization calculations for the operational parameters, based on the refined reactor model. The optimal flue gas inlet velocity was in the range of 20–25 $m \cdot s^{-1}$, whereas the optimal carrier gas inlet velocity was in the range of 9–15 $m \cdot s^{-1}$. Within these ranges, extended mineralization reaction times can be achieved, ensuring the effective separation of mineralized coal fly ash particles from the flue gas stream.

Overall, our study represents a comprehensive effort toward the design and optimization of a fluidized-bed reactor tailored for CO_2 mineralization. This study provides a theoretical foundation for research on waste reclamation and carbon mitigation.

Acknowledgments

The work described in this paper was financially supported by the National Natural Science Foundation of China (NSFC) (Grant No.: 52236004). We also acknowledge the non-carbon energy conversion and utilization institute under the Shanghai Class IV Peak Disciplinary Development Program.

CRediT authorship contribution statement

Duoyong Zhang: Investigation, Methodology, Writing - Original Draft, Visualization, Formal analysis.**: Chen Zhang** Methodology, Writing - Review & Editing, Validation. **Tao Xuan:** Methodology, Writing - Review & Editing. **Xinqi Zhang**: Writing - Review & Editing. **Liwei Wang:** Conceptualization, Resources, Writing - Review & Editing, Supervision, Project administration. **Yongqiang Tian:** Writing - Review & Editing. **Jinqing Zhu:** Writing - Review & Editing.

Competing interests

All authors declare that there are no competing interests.

Reference

[1] S.Y. Chen, J.F. Liu, Q. Zhang, et al., A critical review on deployment planning and risk analysis of carbon capture, utilization, and storage (CCUS) toward carbon neutrality, Renew. Sustain. Energy Rev. 167 (2022) 112537.

[2] B. Dutcher, M.H. Fan, A.G. Russell, Amine-based CO_2 capture technology development from the beginning of 2013—a review, ACS Appl. Mater. Interfaces 7 (2015) 2137–2148.

[3] S.C. Ma, B. Zang, H.H. Song, et al., Research on mass transfer of CO_2 absorption using ammonia solution in spray tower, Int. J. Heat Mass Transf. 67 (2013) 696–703.

[4] G.K. Cui, J.J. Wang, S.J. Zhang, Active chemisorption sites in functionalized ionic liquids for carbon capture, Chem. Soc. Rev. 45 (2016) 4307–4339.

[5] N. Abuelnoor, A. AlHajaj, M. Khaleel, et al., Activated carbons from biomass-based sources for CO_2 capture applications, Chemosphere 282 (2021) 131111.

[6] M. Younas, M. Rezakazemi, M. Daud, et al., Recent progress and remaining challenges in post-combustion CO_2 capture using metal-organic frameworks (MOFs), Prog. Energy Combust. Sci. 80 (2020) 100849.

[7] A.I. Osman, M. Hefny, M.I.A. Abdel Maksoud, et al., Recent advances in carbon capture storage and utilisation technologies: a review, Environ. Chem. Lett. 19 (2021) 797–849.

[8] A. Dindi, D.V. Quang, L.F. Vega, et al., Applications of fly ash for CO_2 capture, utilization, and storage, J. CO_2 Util. 29 (2019) 82–102.

[9] L. Ji, H. Yu, B. Yu, et al., Integrated absorption‑mineralisation for energy-efficient CO_2 sequestration: Reaction mechanism and feasibility of using fly ash as a feedstock, Chem. Eng. J. 352 (2018) 151–162.

[10] I. Ngo, L.Q. Ma, J.T. Zhai, et al., Enhancing fly ash utilization in backfill materials treated with CO_2 carbonation under ambient conditions, Int. J. Min. Sci. Technol. 33 (2023) 323–337.

[11] Z.S. Ding, X. Zhang, T.L. Cheng, et al., Unlocking high carbonation efficiency: Direct CO_2 mineralization with fly ash and seawater, Chem. Eng. Sci. 282 (2023) 119349.

[12] C. Siriruang, P. Toochinda, P. Julnipitawong, et al., CO_2 capture using fly ash from coal fired power plant and applications of CO_2-captured fly ash as a mineral admixture for concrete, J. Environ. Manag. 170 (2016) 70–78.

[13] T.H. Yin, S.F. Yin, A. Srivastava, et al., Regenerable solvents mediate accelerated low temperature CO_2 capture and carbon mineralization of ash and nano-scale calcium carbonate formation, Resour. Conserv. Recycl. 180 (2022) 106209.

[14] T.S. He, J.B. Li, X.D. Ma, et al., Low temperature thermal treatment of incineration fly ash under different atmospheres and its recovery as cement admixture, Materials (Basel) 16 (2023) 3923.

[15] L. Ji, H. Yu, K.K. Li, et al., Integrated absorption-mineralisation for low-energy CO_2 capture and sequestration, Appl. Energy 225 (2018) 356–366.

[16] J.G. Jiang, X.J. Du, M.Z. Chen, et al., Continuous CO_2 capture and MSWI fly ash stabilization, utilizing novel dynamic equipment, Environ. Pollut. 157 (2009) 2933–2938.

[17] R. Zevenhoven, M. Virtanen, CO_2 mineral sequestration integrated with water-gas shift reaction, Energy 141 (2017) 2484–2489.

[18] N.L. Ukwattage, P.G. Ranjith, S.H. Wang, Investigation of the potential of coal combustion fly ash for mineral sequestration of CO_2 by accelerated carbonation, Energy 52 (2013) 230–236.

[19] L. Cheng, T. Li, T.C. Keener, et al., A mass transfer model of absorption of carbon dioxide in a bubble column reactor by using magnesium hydroxide slurry, Int. J. Greenh. Gas Contr. 17 (2013) 240–249.

[20] D. Legendre, R. Zevenhoven, Image analysis assessment of the effect on mixing on aqueous dissolution of CO_2 and air bubble swarms in a bubble column, Chem. Eng. Res. Des. 146 (2019) 379–390.

[21] A. Di Nardo, G. Calchetti, A. Di Carlo, et al., Sorption enhanced steam methane reforming in a bubbling fluidized bed reactor: Simulation and analysis by the CPFD method, Comput. Chem. Eng. 169 (2023) 108080.

[22] J.L. Ma, P. Mahapatra, S.E. Zitney, et al., D-RM Builder: a software tool for generating fast and accurate nonlinear dynamic reduced models from high-fidelity models, Comput. Chem. Eng. 94 (2016) 60–74.

[23] H.L. Duan, K. Zhu, H.F. Lu, et al., CO_2 absorption performance in a rotating disk reactor using DBU-glycerol as solvent, Chin. J. Chem. Eng. 28 (2020) 104–113.

[24] M.H. Wang, A.S. Joel, C. Ramshaw, et al., Process intensification for post-combustion CO_2 capture with chemical absorption: a critical review, Appl. Energy 158 (2015) 275–291.

[25] P. Babu, R. Kumar, P. Linga, Pre-combustion capture of carbon dioxide in a fixed bed reactor using the clathrate hydrate process, Energy 50 (2013) 364–373.

[26] R. Liu, X.L. Wang, S.W. Gao, CO_2 capture and mineralization using carbide slag doped fly ash, Greenh. Gases Sci. Technol. 10 (2020) 103–115.

[27] A. Perejón, L.M. Romeo, Y. Lara, et al., The Calcium-Looping technology for CO_2 capture: On the important roles of energy integration and sorbent behavior, Appl. Energy 162 (2016) 787–807.

[28] J. Adánez, A. Abad, T. Mendiara, et al., Chemical looping combustion of solid fuels, Prog. Energy Combust. Sci. 65 (2018) 6–66.

[29] J.C. Abanades, E.J. Anthony, D.Y. Lu, et al., Capture of CO_2 from combustion gases in a fluidized bed of CaO, AlChE. J. 50 (2004) 1614–1622.

[30] F. Fang, Z.S. Li, N.S. Cai, Continuous CO_2 capture from flue gases using a dual fluidized bed reactor with calcium-based sorbent, Ind. Eng. Chem. Res. 48 (2009) 11140–11147.

[31] M. Nouri, G. Rahpaima, M.M. Nejad, et al., Computational simulation of CO_2 capture process in a fluidized-bed reactor, Comput. Chem. Eng. 108 (2018) 1–10.

[32] S. Wang, Y.S. Shen, Coarse-grained CFD-DEM modelling of dense gas-solid reacting flow, Int. J. Heat Mass Transf. 184 (2022) 122302.

[33] D. Legendre, R. Zevenhoven, A numerical Euler‐Lagrange method for bubble tower CO_2 dissolution modeling, Chem. Eng. Res. \& Des. 111 (2016) 49–62.

[34] Y.F. Guo, C.H. Li, S.X. Lu, et al., K_2CO_3-modified potassium feldspar for CO_2 capture from post-combustion flue gas, Energy Fuels 29 (2015) 8151–8156.

[35] K.W. Chu, B. Wang, D.L. Xu, et al., CFD‐DEM simulation of the gas‐solid flow in a cyclone separator, Chem. Eng. Sci. 66 (2011) 834–847.

[36] Y. Guo, K.D. Kafui, C.Y. Wu, et al., A coupled DEM/CFD analysis of the effect of air on powder flow during die filling, AlChE. J. 55 (2009) 49–62.

[37] W.L. Li, J.H. Wang, Y.C. Lu, et al., CFD analysis of CO_2 absorption in a microporous tube-in-tube microchannel reactor with a novel gas-liquid mass transfer model, Int. J. Heat Mass Transf. 150 (2020) 119389.

Declaration of interests

☒ The authors declare that they have no known competing financial interests or personal relationships that could have appeared to influence the work reported in this paper.

☐The authors declare the following financial interests/personal relationships which may be considered as potential competing interests: